Electrochimica Acta 512 (2025) 145440

Contents lists available at ScienceDirect

Electrochimica Acta

journal homepage: www.journals.elsevier.com/electrochimica-acta

Pitch-derived C coated three-dimensional CNTs/reduced graphene oxide microsphere encapsulating Si nanoparticles as anodes for lithium-ion batteries

Jae Seob Lee [a,b,1], Beom Su Jo [a,1], Jin-Sung Park [c,*], Jung Sang Cho [a,d,e,*]

[a] Department of Engineering Chemistry, Chungbuk National University, Chungbuk 28644, Republic of Korea
[b] Department of Materials Science and Engineering, Korea University, Anam-Dong, Seongbuk-Gu, Seoul 02841, Republic of Korea
[c] Department of Materials Science and Engineering, Ajou University, Suwon 16499, Republic of Korea
[d] Biomedical Research Institute, Chungbuk National University Hospital, Chungbuk 28644, Republic of Korea
[e] Advanced Energy Research Institute, Chungbuk National University, Cheongju, Chungbuk 28644, Republic of Korea

ARTICLE INFO

Keywords:
Silicon
Reduced graphene oxide
Carbon nanotube
Spray drying
Lithium-ion batteries

ABSTRACT

This study presents an innovative strategy for synthesizing a sophisticated three-dimensional conductive framework that contains well-dispersed silicon nanoparticles. This framework features silicon nanoparticles encapsulated by a composite of one-dimensional carbon nanotubes (CNTs), two-dimensional reduced graphene oxide (rGO), and amorphous carbon, all of which are further coated with a pitch-derived carbon (PDC) layer. This unique nanostructured anode was prepared from a one-pot spray drying process, heat-treatment and subsequent pitch-derived carbon coating. Combining 1D CNTs and 2D rGO nanosheets creates a 3D conductive network that can facilitate the electrochemical reaction kinetics. Furthermore, pitch-derived carbon coating at the interior and on the surface densified the electrode, ensuring both lithium-ion and electron transport and enhancing the Coulombic efficiency. Therefore, the composite plays the role of an effective mixed ionic and electronic conductor (MIEC), which can highly enhance the electrochemical performance of Si-based anode. Also, the volume expansion issues of silicon materials could be resolved by compositing with 3D conductive carbon matrix and reinforcing the structural robustness by coating with PDC layer, which could effectively alleviate the stress occurring from repetitive cycling. When used as the anode in lithium-ion batteries, the microspheres exhibited exceptional initial discharge/charge capacities of 3814/2791 mA h g^{-1} at 0.1 A g^{-1} with high Coulombic efficiency of 73.2 %, and demonstrated highly stable cycle performance, delivering a discharge capacity of 947 mA h g^{-1} after 350 cycles at a current density of 1.0 A g^{-1}.

1. Introduction

As the demand for large-scale storage systems, including electric vehicles and energy storage systems continues to rise, the necessity for lithium-ion batteries (LIBs) with high energy density becomes increasingly paramount [1–3]. Graphite is usually adopted as the anode for LIBs, but the theoretical capacity of 372 mA h g^{-1} doesn't seem to be satisfactory considering the large-scale energy storage of futuristic applications [1]. In comparison, silicon has received research highlight since it exhibits almost ten times the theoretical capacity of graphite (Si forms $Li_{22}Si_5$ with capacity of 4212 mA h g^{-1} at high temperature and $Li_{15}Si_4$ with capacity of 3596 mA h g^{-1} at room temperature) [4,5]. In addition, it is characterized by a low electrode potential of approximately 0.4 V vs. Li/Li^+, abundant resources, and environmental benignity, making it a highly promising candidate for the next-generation anode in LIBs [6,7]. However, silicon exhibits low electrical conductivity and undergoes significant volume expansion (300–400 %), which results in the electrode pulverization, delamination of the electrode material from the current collector, and ultimately fast capacity decay [8,9]. In addition, Li^+ loss occurs due to the formation of thick and unstable SEI layer, which results in high irreversible capacity and therefore low Coulombic efficiency [10,11].

To address the aforementioned issues, many efforts have been made to improve the cycle stability as well as the electrical conductivity of the

* Corresponding authors.
E-mail addresses: jinsung@ajou.ac.kr (J.-S. Park), jscho@cbnu.ac.kr (J.S. Cho).
[1] These authors contributed equally to this work.

https://doi.org/10.1016/j.electacta.2024.145440
Received 30 September 2024; Received in revised form 18 November 2024; Accepted 29 November 2024
Available online 30 November 2024

silicon-based anode materials. To enhance the electrical conductivity, silicon anodes have been composited with conductive materials including carbon, metals, conductive polymers, and metal silicides [12–15]. Amongst various materials, conductive carbon including graphene and CNT not only enhances the electrical conductivity and rate performance, but also improves the cycle stability by alleviating the volume changes during cycling [16,17]. As an example, Lu et al. prepared nitrogen-doped graphene cages-encapsulated mesoporous Si spheres (Si@graphene cage) [18]. Due to the graphitic carbon cages with high electrical conductivity, Si-graphene composite anode exhibited much higher capacity in comparison to Si particles without carbonaceous framework and remarkable lifespan, where a capacity of 900 mA h g^{-1} could be achieved after 200 cycles at 1.0 A g^{-1}. The Si-graphene composite anode also exhibited high rate performance, where a high discharge capacity of 890 mA h g^{-1} at 5.0 A g^{-1}. Additionally, there were attempts to physically attach Si nanoparticles on the surface of graphene, which greatly enhance the electrochemical performance [19]. Xiong et al. synthesized CNTs-supported porous silicon microparticles using low-temperature molten salt approach for use as anode in LIBs [20]. CNTs-supported Si anode exhibited excellent electrochemical properties, where 600.5 mA h g^{-1} could be retained after 300 cycles at 1.0 A g^{-1}. However, not many studies have composited both graphene, CNT, and silicon; combining 1D CNT and 2D graphene results in the formation of a 3D conductive network that can highly facilitate the electron transport. In addition, combining the two leads to a denser structure, compared to those composed solely of graphene or CNT, which can enhance the contact with silicon and improve the Coulombic efficiency. As an example of one of the few studies reporting Si/graphene/CNT composite, Cai et al. adopted nanostructured honeycomb silicon wrapped in graphene/CNT system as a highly stable anode for LIBs, which demonstrated the synergy of combining graphene with CNTs in improving the battery performance [21]. At last but not least, Cho et al. has suggested the use of pitch, which is a well-known cheap carbon material derived from petroleum, as a coating material on the surface of silicon particles [22]. Simple heat treatment would lead to a pitch-derived uniform coating layer with high electrical conductivity on the surface, which can effectively suppress the volume expansion of the particles during repetitive cycles.

In this study, a three-dimensional conductive framework composed of 1D CNTs, 2D reduced graphene oxide (rGO), and amorphous carbon (AC) encapsulating Si nanoparticles (Si-CNT/rGO/AC) is prepared from a facile spray drying process as a strategy to overcome the disadvantages of silicon. Here, nano-sized Si particles with sizes between 50 and 100 nm, which have shown the best performance among Si particles with various sizes in a study by Li et al. were adopted for obtaining optimized battery performance [23]. Moreover, guidance on the spray-assisted method for the facile fabrication of microspheres where both CNTs and rGO are effectively integrated to form a 3D conductive matrix in which nanosized silicon particles are uniformly distributed is provided. The strategy introduced in this study enables the production of microspheres through a one-step spray method, which significantly simplifies the synthesis process and provides an efficient approach to integrating CNTs with rGO. CNT/rGO conductive 3D framework that surround the silicon nanoparticles can improve the overall electrical conductivity of the materials and alleviate the volume changes that occur during the lithiation/delithiation of silicon. Lastly, to reduce the void space and minimize the initial irreversible capacities of Si-CNT/rGO/AC microspheres, pitch-derived conductive carbon is evenly coated both inside and outside the nanostructured particles. The integrity of the microspheres during charge and discharge processes is improved due to the pitch-derived carbon (PDC) that fills the pores in the nanostructured framework and forms stable coating on the surface, which results in excellent cycling performance, where a reversible capacity of 947 mA h g^{-1} can be retained after 350 cycles at a current density of 1.0 A g^{-1}.

2. Experimental

2.1. Preparation of Si-CNT/rGO/AC@PDC microspheres

PDC-filled and -coated Si-CNT/rGO/AC (Si-CNT/rGO/AC@PDC) microspheres were prepared by spray-drying process, followed by heat treatment and pitch coating at various ratios. The multi-walled carbon nanotubes (MWCNTs, obtained from Cheap Tubes Inc., Cambridgeport, USA; purity: >95.0 wt.%) were prepared by acid treatment using a mixture of HNO_3 and H_2SO_4. Briefly, 40 and 120 mL of the HNO_3 and H_2SO_4 (1:3 v/v) were used, respectively. Once the temperature reached around 75 ℃, 2.0 g of MWCNTs was added to the acid solution, which is then stirred for 6 h. After acid treatment, the MWCNTs were thoroughly washed four times with distilled water, and acid-treated MWCNTs were obtained by freeze-drying. Additionally, the graphene oxide (GO) nanosheets were prepared from graphite flakes (Sigma-Aldrich) *via* the modified Hummer's method [24]. 0.065 g of acid-treated MWCNT and 0.065 g of GO were dispersed in 60 mL of distilled water by ultrasonication for 3 h until a homogeneous suspension was formed. Then 1.0 g of silicon nanopowder (Luoyang Tongrun Info Technology Co., Ltd., >99 %, ϕ = 50–100 nm) and 1.0 g of sucrose ($C_{12}H_{22}O_{11}$, M_w = 342.3, DAEJUNG, Extra Pure) were added to the suspension, followed by ultrasonication and stirring for 3 h. The colloidal solution was pumped at a speed of 2.6 mL min^{-1} to a two-fluid nozzle, where it was atomized at a pressure of 0.2 bar. The temperatures at the inlet and outlet of spray dryer were 190 ℃ and 100 ℃, respectively. The spray-dried powder was heat-treated at 800 ℃ for 4 h under N_2 atmosphere, where the ramping rate was 5 ℃ min^{-1}. For pitch-derived carbon coating, bulk pitch powder was added to the Si-CNT/rGO/AC microspheres such that the pitch constituted 10, 30, and 50 wt.% of the combined total weight, to optimize the PDC coating layer. For PDC coating, bulk pitch powder was dissolved in tetrahydrofuran (THF) solvent. Several drops of pitch-THF solution were dropped onto Si-CNT/rGO/AC microspheres so the powder can be absorbed in the solution. The slurry was physically mixed using an agate mortar, and dried in air atmosphere. The dried mixture was then carbonized at 900 ℃ in a N_2 atmosphere for 3 h to form pitch-derived conductive carbon. The preparation procedure for Si-CNT/AC microspheres are similar to that of the Si-CNT/rGO/AC microsphere, however, the procedure differs in way that GO nanosheets were not added to the spray solution.

2.2. Characterization techniques

The morphologies of Si-CNT/rGO/AC@PDC, Si-CNT/rGO/AC, and Si-CNT/AC microspheres were examined using microscopic characterization techniques including field emission scanning electron microscopy (FE-SEM, ULTRA PLUS, ZEISS) and field emission transmission electron microscopy (FE-TEM, JEOL, JEM-2100F) at the Korea Basic Science Institute (Daegu). The chemical nature of Si-CNT/rGO/AC@PDC microspheres was investigated using X-ray photoelectron spectrometer (XPS, K-Alpha, Thermo Fisher Scientific) with Al K_α radiation (12 kV, 20 mA). The crystal phases of the prepared samples were characterized by powder X-ray diffraction (XRD, D8 Discover with GADDS, Bruker). The surface areas and pore sizes were investigated by using the adsorption-desorption isotherm and Barrett–Joyner–Halenda (BJH) approaches with pure N_2 as the adsorbate gas. Thermogravimetric analysis (TGA, Pyris 1, PerkinElmer) was performed in the temperature range of 25–800 ℃ at a ramp rate of 10 ℃ min^{-1} in air to confirm the carbon content of the composites. Raman spectroscopy (Horiba Jobin-Yvon, HR800, LabRam) was performed for analyzing the structure of silicon and carbon present in the samples. In addition, elemental analysis (EA, vario MICRO cube, Elementar) technique based on a high temperature (1200–1400 ℃) combustion method was used to quantify the amount of carbon and nitrogen elements in the synthesized samples.

2.3. Electrochemical measurements

A typical slurry-casting method was utilized to prepare anode by mixing the as-prepared powders as the active material, super-P as a conductive agent, and poly(acrylic acid) as a binder in a mass ratio of 6:2:2 in a minimum amount of deionized water. Then prepared slurry was coated onto a copper current collector and dried overnight in a hot-air oven at 60 ℃. The dried coated slurry was punched into circular electrodes (ϕ = 14 mm) with an average active material loading of 0.8 mg cm^{-2} and transferred to a glove box. The active material loading was consistently maintained throught all experiments. CR2032 coin cells were assembled using the prepared electrodes as anodes, metallic Li as the counter electrode, and microporous polypropylene film as a separator. The electrolyte consisted of 1.15 M $LiPF_6$ in a blend of ethylene carbonate (EC), diethyl carbonate (DEC) and dimethyl carbonate (DMC) in a 2:4:4 vol ratio with 1.0 wt.% of vinylene carbonate (VC), 1.0 wt.% $LiPO_2F_2$ and 12.5 wt.% of fluoroethylene carbonate (FEC) as an additive. The rate capabilities of the assembled cells were measured at various current densities ranging from 0.1 to 5.0 A g^{-1} using a WBCS3000 (WonATech) battery cycler at 25 ℃. The cycling performance of the assembled cells was evaluated at 1.0 A g^{-1}. Cyclic voltammetry (CV) curves were obtained at a voltage scan rate of 0.1 mV s^{-1} in the voltage window of 0.01–1.2 V. Electrochemical impedance spectroscopy (EIS, ZIVE SP1) measurement was employed to obtain Nyquist plots in the frequency range of 100 kHz–0.01 Hz.

3. Results and discussion

A schematic illustration for the preparation procedure of Si-CNT/rGO/AC@PDC microspheres by a one-pot spray drying process, heat-treatment and pitch-derived carbon coating is shown in Scheme 1. Firstly, colloidal CNTs and GO nanosheets used in this research were prepared from acid-treatment and modified Hummer's method, respectively. Morphologies of the prepared GO nanosheets and CNTs investigated with FE-SEM are shown in Fig. S1a and b. In addition, the size of the Si nanoparticles dispersible in distilled water and their size distribution was confirmed by FE-SEM images to be between 50 and 100 nm (Fig. S1c). The XRD pattern of the Si nanoparticles were also

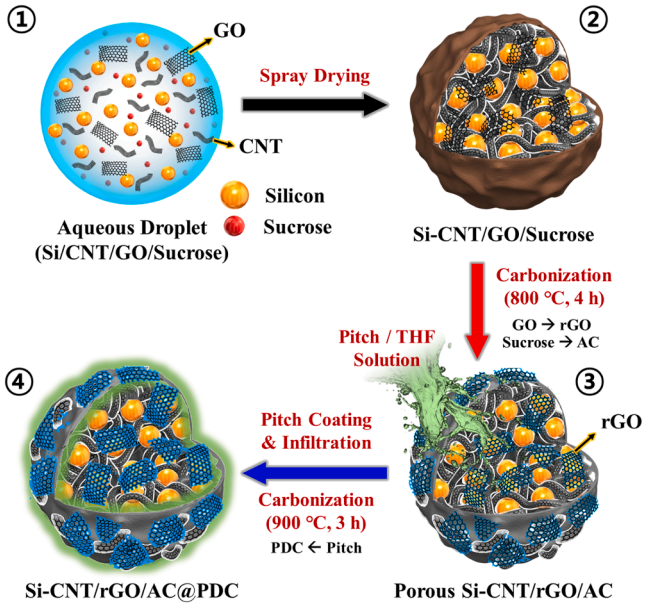

Scheme 1. Schematic representation of formation mechanism (①–④) of 3D conductive framework composed of 1D CNTs, 2D rGO, and amorphous carbon encapsulating Si nanoparticles and imbued with pitch-derived carbon (Si-CNT/rGO/AC@PDC microspheres).

obtained, where clear peaks corresponding to Si (JCPDS #01-0787) could be observed (Fig. S1d). Aqueous colloidal solution used for the spray drying process was obtained by adding Si nanoparticles, GO nanosheets, CNTs, and sucrose in distilled water and subsequent ultrasonication for obtaining a homogeneous suspension. The schematic diagram showing the spray drying system used in this research is shown in Scheme S1. One-pot spray drying of the aqueous colloidal solution yielded Si-CNT/GO/sucrose composite microspheres, which is characterized by well-distributed Si nanoparticles inside 3D carbonaceous framework, which is comprised of 1D CNTs and 2D GO nanosheets. Porous Si-CNT/rGO/AC microspheres were prepared from a one-step heat treatment under N_2 atmosphere. During carbonization heat-treatment, graphene oxide was reduced to form reduced graphene oxide (rGO), and sucrose was transformed into amorphous carbon (AC). The overall porosity of the microspheres increased due to the carbonization and thermal contraction of sucrose, which created voids between the silicon particles, resulting in a porous structure. Then, a set amount of THF solution to which pitch carbon is evenly dispersed was infiltrated in porous Si-CNT/rGO/AC microspheres for forming a conductive pitch-derived carbon (PDC) layer on both inside and outside the nano-structured particles. The pitch-derived carbon layer serves the following purposes: 1) to further reinforce the structural robustness of the electrode that contains Si nanoparticles by alleviating the volume changes that occur during repetitive cycling [25], and 2) densify the nano-structured anode material by reducing the void space and therefore minimize the irreversible capacities of the electrode [26]. The weight percentage of pitch to Si-CNT/rGO/AC microspheres was set as 10 wt.%, 30 wt.%, and 50 wt.% in order to determine the optimum amount of pitch carbon that results in the best electrochemical performance. During the carbonization heat treatment, pitch is transformed into conductive carbon, and Si-CNT/rGO/AC@PDC could be obtained.

The morphologies, XRD and Raman characterization of Si-CNT/GO/sucrose composite microspheres prepared from spray drying process are shown in Fig. S2. As can be observed in the FE-SEM image in Fig. S2a, Si-CNT/GO/sucrose composite microspheres exhibited independent microspherical morphologies, without aggregation characteristics between each microsphere. The FE-SEM image of a single microsphere in Fig. S2b shows nanosized silicon particles composited with GO nanosheets and nanosized CNTs. Nanosized CNTs and GO nanosheets are indicated by green and blue arrows, respectively. Peaks corresponding to Si material could be easily discerned in the XRD pattern in Fig. S2c. In addition, peaks corresponding to CNT/GO materials could also be discerned, indicating the presence of CNTs and GO nanosheets. In the Raman spectrum in Fig. S2d, three peaks could be observed at 518, 1350, and 1592 cm^{-1}, which can be assigned to the Si—Si bond and D and G bands of carbon, respectively [27,28]. The degree of graphitization in carbon material is generally assessed by examining the intensity ratio of the D-band (I_D) to that of the G-band (I_G). The I_D/I_G ratio was calculated to be 0.85, which indicates highly graphitic nature of carbon in Si-CNT/GO/sucrose composite microspheres. The microspheres went through carbonization heat treatment, which yielded porous Si-CNT/rGO/AC microspheres. Comprehensive materials characterization of the microspheres including FE-SEM, TEM, and HR-TEM images, SAED and XRD patterns, TGA and Raman analyses are altogether showcased in Fig. 1. The FE-SEM images of Si-CNT/rGO/AC microspheres shown in Fig. 1a and b exhibited independent microspherical morphology, which is inherited from Si-CNT/GO/sucrose composite microspheres. It is notable that the size of the spheres decreased from 3.54 μm to 2.44 μm due to the thermal shrinkage during the carbonization process from the spray-dried Si-CNT/rGO/AC microspheres to their Si-CNT/rGO/AC counterpart. The TEM image shown in Fig. 1c clearly shows Si nanoparticles evenly distributed within a single microsphere. In the magnified TEM image in Fig. 1d, it is observed that the Si nanoparticles are encapsulated by the rGO nanosheets, which is further integrated with CNT units. The HR-TEM image of the microsphere shown in Fig. 1e revealed lattice fringes separated by 0.31 and

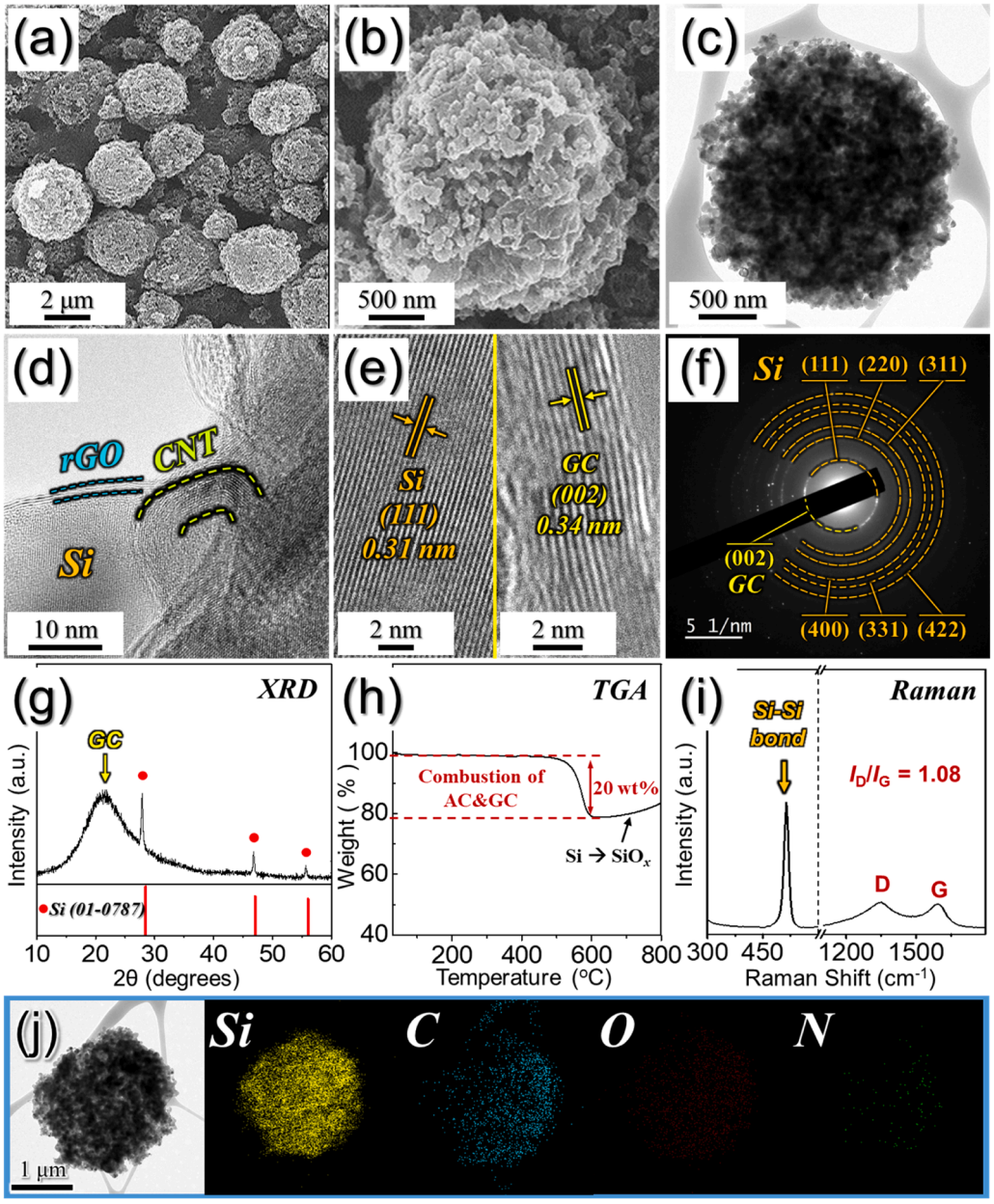

Fig. 1. Physical characterizations of porous Si-CNT/rGO/AC microsphere prepared by spray drying and subsequent carbonization at 800 ℃: (a, b) FE-SEM images, (c, d) TEM image, (e) HR-TEM images, (f) SAED pattern, (g) XRD pattern, (h) TG curve, (i) Raman spectrum, and (j) elemental dot mapping images.

0.34 nm, corresponding to the (111) and (002) planes of Si and graphitic carbon, respectively. The SAED pattern shown in Fig. 1f revealed numerous crystallographic rings that correspond to the (111), (220), (311), (400) (331) and (422) planes of Si and (002) plane of graphitic carbon. Again, three characteristic peaks corresponding to Si material and a peak at 21.2° corresponding to graphitic carbon could be observed in the XRD pattern (Fig. 1g). TGA curves in Fig. 1h revealed two step weight changes with the increase in temperature; The weight loss that occurs between 500 and 570 ℃ correspond to the combustion of amorphous carbon and graphitic carbon [29–32]. From the TGA curve data, it was made clear that carbon takes up 20 wt.% in porous Si-CNT/rGO/AC microspheres. This is further confirmed with the data obtained from elemental analysis (Table S1), which revealed that the carbon content in the microspheres is 20.5 wt.%. The gradual weight increase that is observed at temperatures higher than 600 ℃ can be attributed to the transition from Si to SiO_x. Raman spectrum also revealed peaks corresponding to Si—Si bond and D and G bands of carbon (Fig. 1i) [27,28]. The I_D/I_G value of porous Si-CNT/rGO/AC microspheres was 1.08, which is a higher value than that of Si-CNT/GO/sucrose composite microspheres. This could be attributed to the formation of amorphous carbon with numerous defects and the reduction of graphene oxide nanosheets during carbonization heat-treatment. The elemental dot mapping images of porous Si-CNT/rGO/AC microspheres is provided in Fig. 1j, where the homogeneous distribution of Si nanoparticles in CNT/rGO/AC matrix could be confirmed. To prove the high degree of dispersion between the particles and the effective combination of different substances during the preparation steps, low-magnification TEM image and the elemental dot mapping images corresponding to Si, C, O, and N elements were obtained and shown in Fig. S3. As can be seen in the elemental mapping images, the homogeneous dispersion of Si nanoparticles within microspheres could be well confirmed. In addition, the dots corresponding to C and the O elements well demonstrate the even dispersion of carbonaceous substances within the microspheres as well.

To enhance the electrical conductivity and obtain optimized electrochemical properties, porous Si-CNT/rGO/AC microspheres to which THF solution containing pitch carbon was infiltrated and heat treated to form Si-CNT/rGO/AC@PDC microspheres. The infiltration of THF solution (with fluidic characteristics) that contains pitch carbon to the interior resulted in the formation of PDC layer on both inside and the surface of the microspheres. Si-CNT/rGO/AC microspheres were coated with pitch carbon in varying weight percentages (10, 30, and 50 wt.%), which are denoted as @PDC-10, @PDC-30, and @PDC-50, respectively. As shown in the TEM images in Fig. 2a–c, it is clearly seen that the higher the amount of pitch carbon is used to coat the microsphere, the darker it appears in the TEM images. Compared to Fig. 1c, where numerous void spaces can be observed in a single particle, it is clear that pitch-derived carbon was successfully infiltrated into the interior and coated on the surface of the Si-CNT/rGO/AC microspheres, densifying the anode particles. The TGA results of @PDC-10, @PDC-30, and @PDC-50 are shown in Fig. 2d–f, where the carbon content in each sample is determined to be 22, 28, and 39 wt.%, respectively. Moreover, the carbon content in each samples obtained from the TG results is summarized in Table S2 to clearly reveal the variation of carbon content in the samples obtained before and after PDC coating according to the pitch content. The results well-matched with the elemental analysis data of the microspheres shown in Table S1 and Fig. S4, where the carbon content in each sample was determined to be 23.0, 28.5, and 38.6 wt.%, respectively. All the samples exhibited weight increase at temperatures higher than 650 ℃, where the extent of the weight increase decreased with a greater amount of PDC coating since the relative amount of Si nanoparticles decreased. Coin cells were assembled using Si-CNT/rGO/AC microspheres with varying amount of PDC coating to determine the optimum coating thickness. Upon increasing the amount of pitch carbon from 10 to 30 wt.%, rise in capacity could be observed (Fig. 2g). However, when the amount of pitch carbon increased from 30 to 50 wt.%, a large drop in capacity could be observed. In terms of cycle performance, Si-CNT/rGO/AC@PDC-30 microspheres exhibited more stable cycle performance in comparison to Si-CNT/rGO/AC@PDC-10 microspheres. The increase in stability is attributed to the higher amount of carbon coating, which effectively alleviated the volume expansion during repetitive cycles. As a result, a high capacity of 947 mA h g^{-1} could be maintained after 350 cycles at 1.0 A g^{-1}. The details of the electrochemical performance will be discussed further in later section. The optimal quantity of pitch-derived carbon coated on Si-CNT/rGO/AC microspheres allows the formation of highly dense 3D conductive carbon framework, which can facilitate the contact between the rGO/CNT matrix with Si nanoparticles, resulting in both high capacity and cycle performance. Therefore, 30 wt.% pitch coating was selected as the optimum coating amount.

The morphology of Si-CNT/rGO/AC@PDC-30 microspheres was investigated by FE-SEM and is shown in Fig. 3a and b. The average diameter of the prepared microspheres with non-aggregated characteristics was 2.2 μm. Since the interior and the outer surface of microspheres are coated with 30 wt.% pitch carbon, Si-CNT/rGO/AC@PDC-30 microspheres appear denser in comparison to uncoated microspheres (Fig. 1b and c) as shown electron micrographs in Figs. 3b and 2b. TEM image reveals the presence of Si nanoparticles, CNT, rGO, and PDC layer coated on the surface with thickness of 6.5 nm (Fig. 3c). To get a better understanding, HR-TEM images were obtained where PDC coating layer on the surface of Si nanoparticles and graphitic carbon can be discerned (Fig. 3d). Here, lattice fringe distances of 0.31 and 0.34 nm corresponding to the (111) and (002) planes of Si and graphitic carbon, respectively, could be observed. The presence of Si nanoparticles and graphitic carbon is further verified by the SAED pattern and XRD pattern (Fig. 3e and f). I_D/I_G value of Si-CNT/rGO/AC@PDC microspheres was calculated as 1.10, which is slightly higher than that of microspheres without PDC coating layer (Fig. 3g). During the carbonization process, pitch carbon functional groups undergo pyrolysis, which results in the formation of additional defects. Furthermore, some disordered carbon

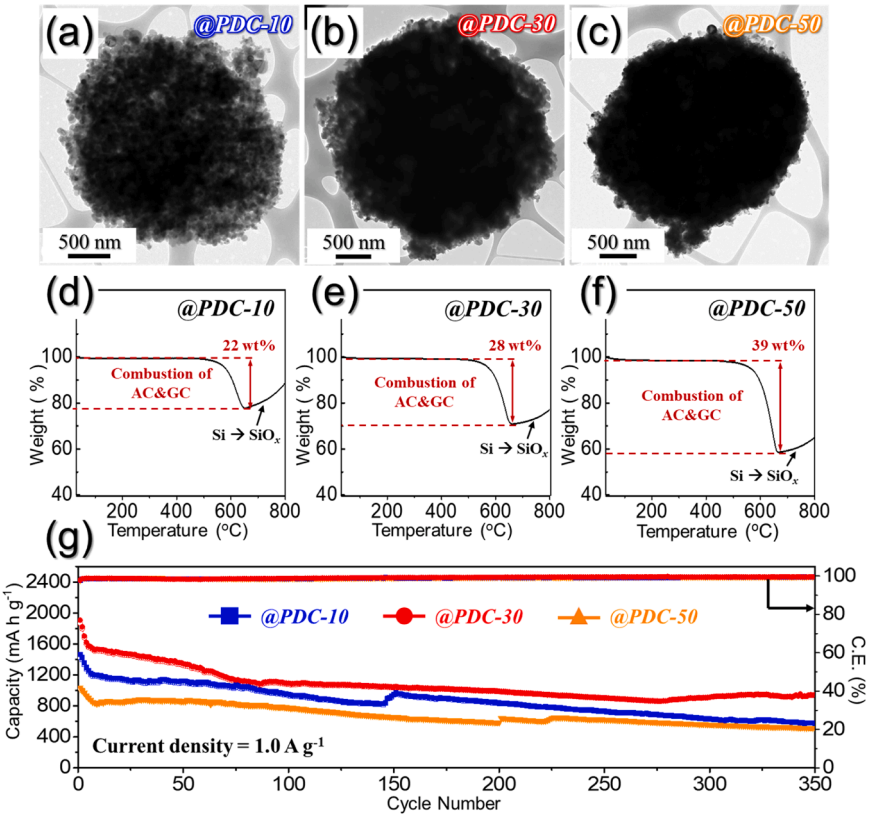

Fig. 2. (a–c) FE-SEM images, (d–f) TG curves, and (g) cycling performance of Si-CNT/rGO/AC@PDC microspheres synthesized with different amounts of pitch powder at a current density of 1.0 A g^{-1}; (a, d) 10 wt.%, (b, e) 30 wt.%, and (c, f) 50 wt.%.

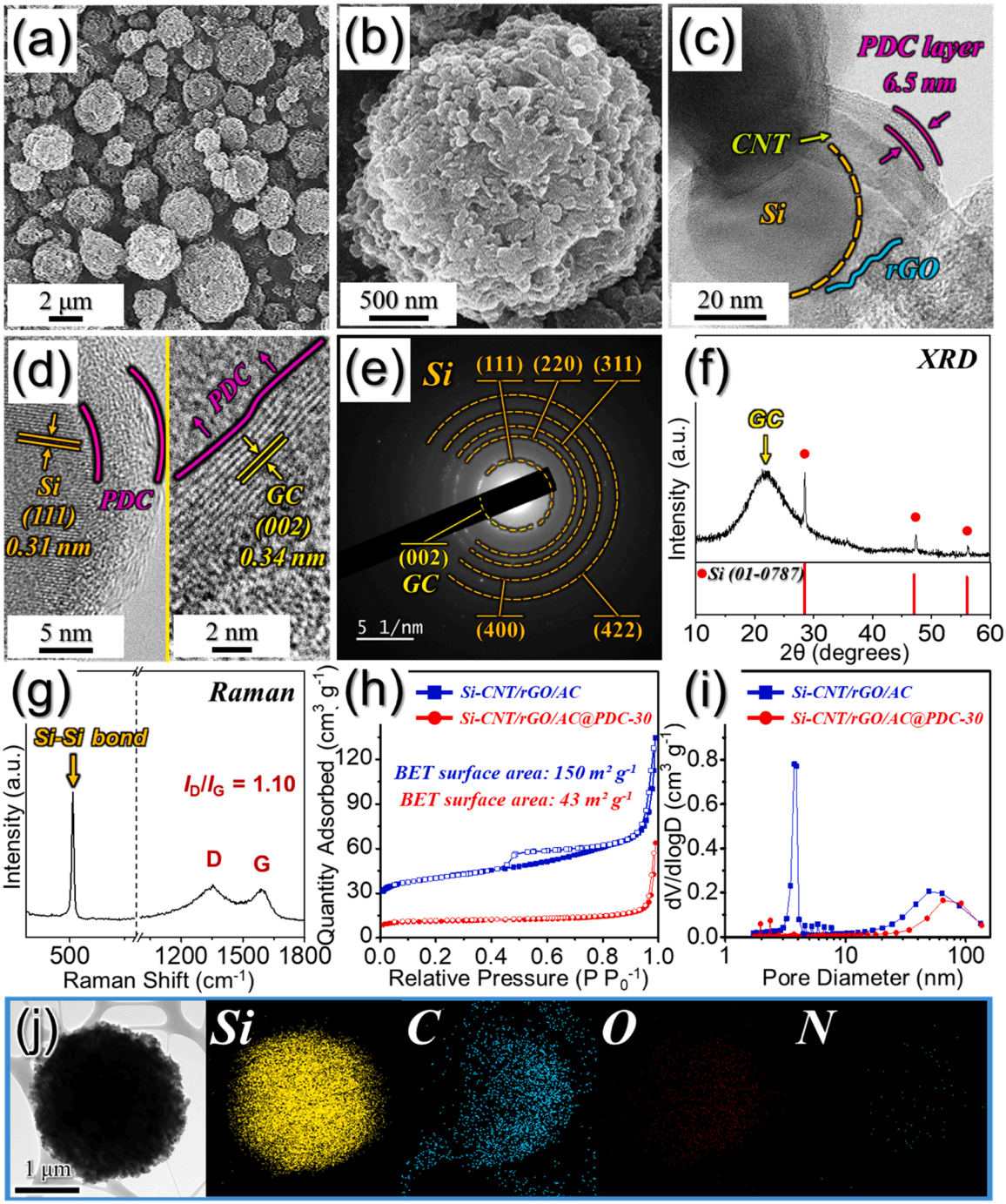

Fig. 3. Physical characterizations of Si-CNT/rGO/AC@PDC-30 microsphere: (a, b) FE-SEM images, (c) TEM image, (d) HR-TEM images, (e) SAED pattern, (f) XRD pattern, (g) Raman spectrum, (h) N_2 adsorption-desorption isotherm, (i) BJH pore-size distribution, and (j) elemental dot mapping images.

structures are also formed during the heat treatment, which altogether led to the increase in I_D/I_G value. BET surface areas of Si-CNT/rGO/AC and Si-CNT/rGO/AC@PDC-30 microspheres determined from N_2 adsoprtion-desorption isotherms were 150 and 43 $m^2\ g^{-1}$, respectively (Fig. 3h). The isotherm of Si-CNT/rGO/AC microspheres revealed a clear H3 hysteresis loop, which is indicative of the presence of mesopores. This can be also confirmed from the BJH pore size analysis, which revealed a distinct peak of ~ 2.5 nm, corresponding to small mesopores in the sample (Fig. 3i). In addition, a broad peak centered at 50 nm could also be observed, which can be attributed to the following reasons: 1) Entanglement of CNT bundles, 2) stacking and folding of rGO nanosheets, 3) the interactions between the individual components of the Si-CNT/rGO/AC composite, especially between Si nanoparticles, CNT, and rGO. After the pitch coating and subsequent carbonization process, pitch-derived carbon layer was formed at the interior and the outer surface of Si-CNT/rGO/AC microspheres, reducing the pore within the nanostructured framework and decreasing the specific surface area. This result indicates that the mesopores smaller than 10 nm, notably ~2.5 nm, within the Si-CNT/rGO/AC composite are filled due to capillary action of pitch during the pitch coating process. This is corroborated by the BJH analysis of Si-CNT/rGO/AC@PDC-30 microspheres. Moreover, the amount of relatively larger pores also decreased due to the pitch-carbon coating layer. The elemental dot mapping images again revealed the homogeneous distribution of Si nanoparticles in the carbon

matrix (Fig. 3j). The chemical nature of the prepared Si-CNT/rGO/AC@PDC-30 microspheres was elucidated with the XPS analysis (Fig. 4). In the survey scan, Si 2*p*, C 1*s*, and O 1*s* peaks could be found, which is in line with the components in the microspheres (Fig. 4a). In the Si 2*p* spectrum shown in Fig. 4b, two peaks at 98.7 and 99.3 eV could be found, which correspond to the $2p_{3/2}$ and $2p_{1/2}$ Si, respectively [33]. Numerous peaks centered at 102.5, 102.9, 103.5, and 104.2 eV could also be found, which can be assigned to Si^{+}, Si^{2+}, Si^{3+}, and Si^{4+}, respectively, which can attributed to the thin silica film on the Si surface [33]. C 1s spectrum (Fig. 4c) also revealed peaks corresponding to C═C (283.6 eV), C—C (284.6 eV), C—O (285.7 eV), C═O (288.0 eV), and O—C═O (289.4 eV) bond in CNT, rGO, amorphous carbon, and pitch-derived carbon materials [34–36].

The electrochemical performance of Si-CNT/rGO/AC@PDC-30, Si-CNT/rGO/AC, and Si-CNT/AC microspheres as anode materials in LIBs

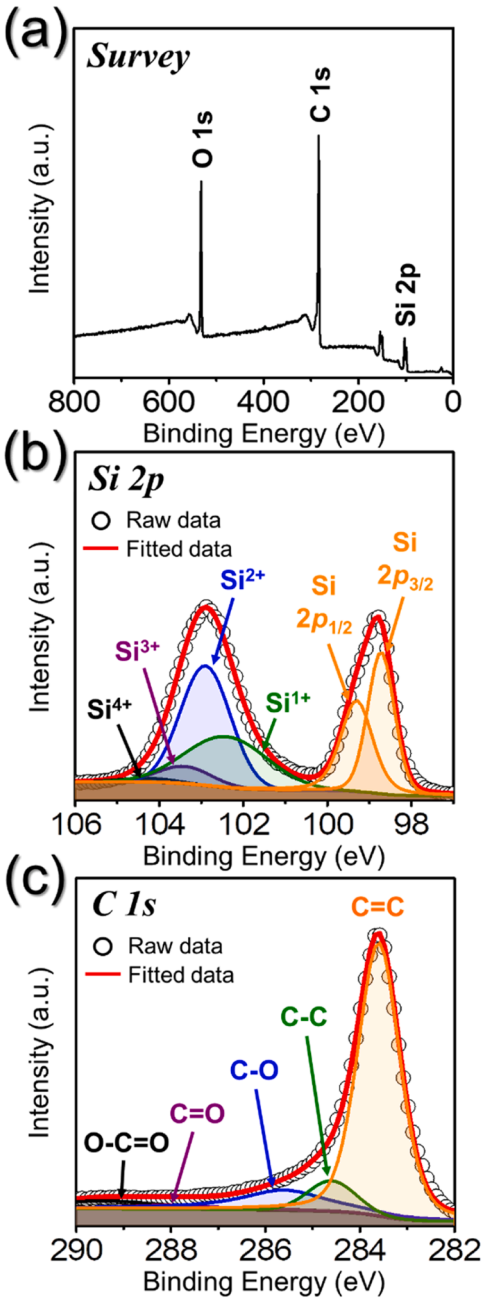

Fig. 4. (a) XPS survey spectrum, (b) Si 2*p*, and (c) C 1*s* XPS spectrum of Si-CNT/rGO/AC@PDC-30 microsphere.

are systematically investigated and presented in Fig. 5. Si-CNT/AC microspheres were prepared with the identical procedure except that graphene oxide nanosheets were not added to the spray drying precursor solution. The microspheres were prepared for comparison purpose for evaluating the synergistic effect of combining CNTs and graphene in comparison to when only using CNT material. The morphology of Si-CNT/sucrose composite microspheres was examined by FE-SEM as shown in Fig. S5a, where silicon nanoparticles and nanosized CNTs could be well observed. After carbonization process, the presence of spherical silicon nanoparticles could be explicitly observed due to the thermal decomposition of sucrose (Fig. S5b). TEM imaging of the microspheres (Fig. S5c) confirmed the porous interior of Si-CNT/AC microspheres, where silicon particles are well composited with amorphous carbon and CNTs. The co-existence of Si nanoparticles and CNTs can also be confirmed from the HR-TEM images, SAED pattern and XRD pattern of the composite (Fig. S5d–f). The TGA curves of the composite revealed that the carbon content in Si-CNT/AC microspheres is 20 wt.%; for the synthesis of Si-CNT/AC microspheres, double the amount of CNTs was used to compensate for the graphene oxide nanosheets (Fig. S5g). This is further confirmed by the elemental analysis data in Table S1, where the carbon content was determined as 20.7 wt.%. The BET surface area of the composite microsphere was determined to be 178 $m^2\ g^{-1}$ using the N_2 adsorption/desorption isotherm (Fig. S5h). From the shape of the isotherm, the presence of mesopores could be inferred, which is ascertained with the BJH pore size distribution (Fig. S5i). The presence of small and large-sized mesopores can be attributed to the entangled nano-sized CNTs and the pores between the Si nanoparticles and CNTs. One-pot spray drying of the colloidal solution that contains Si nanoparticles and CNTs resulted in the well-distributed Si particles in the entangled conductive carbon matrix, which can be further confirmed with the elemental dot mapping images (Fig. S5j). The cyclic voltammetry (CV) curves of Si-CNT/rGO/AC@PDC-30, Si-CNT/rGO/AC, and Si-CNT/AC microspheres were obtained at a scan rate of 0.1 mV s^{-1} in the voltage range between 0.01 and 1.2 V for the initial 5 cycles and shown in Figs. 5a and S6. In the initial cathodic scan, broad peaks could be discerned, which can be ascribed to the formation of solid-electrolyte interphase (SEI) layer on the anode materials, which are not observed in the subsequent cycles [37]. The large peaks that occur in the cathodic sweep at voltages lower than 0.3 V correspond to the alloying reaction between Li and Si to form lithium silicide (Li_xSi). During the initial anodic scan, two major peaks are observed at 0.34 and 0.53 V, which can be attributed to the step-by-step delithiation of Li_xSi, leading to the formation of silicon [38,39]. In the subsequent cycles, major peaks occurred at 0.2 and near 0 V in the cathodic sweep, which correspond to the gradual increase of x in Li_xSi. Anodic peaks in the following cycles also occurred at 0.34 and 0.53 V, in line with the CV curves in the initial cycle. The evolution of both anodic and cathodic peaks after the initial scan with higher intensity could be observed, which can be attributed to the gradual activation of Si materials in the anode during repetitive charge and discharge processes [40,41]. On the other hand, the cathodic peak intensities of the first two cycles did not increase due to the formation of SEI layer on the surface on the Si during the initial cycles. Briefly, this is a result that a portion of the lithium ions was consumed in forming the SEI layer, which reduces the contribution from lithium insertion into the Si material in the initial cycle. After the stabilization of SEI layer, the more efficient lithium insertion/extraction processes leads to the ongoing activation of the Si material. This behavior highlights the critical role of SEI formation and activation processes in defining the electrochemical behavior of the Si material during the initial cycles [42]. The initial discharge-charge curves of Si-CNT/rGO/AC@PDC-30, Si-CNT/rGO/AC, and Si-CNT/AC microspheres were recorded at a current density of 0.1 A g^{-1} and shown in Fig. 5b. During the initial discharge process, gradual capacity rise could be observed starting from 1.25 V due to the formation of SEI layer on the surface of the anode. Very long plateaus could be observed at voltage lower than 0.1 V due to the lithiation of silicon to form Li_xSi. During the charging step, plateaus

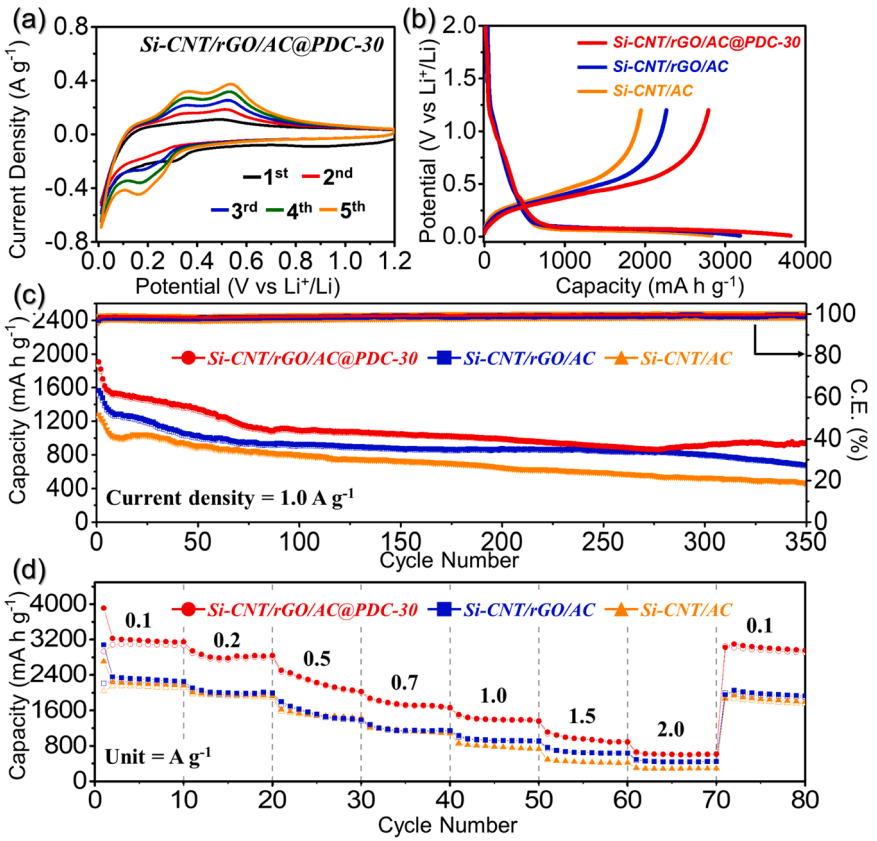

Fig. 5. Electrochemical properties of Si-CNT/rGO/AC@PDC-30, Si-CNT/rGO/AC, and Si-CNT/AC microspheres: (a) CV curves of Si-CNT/rGO/AC@PDC-30 microsphere, (b) initial Galvanostatic discharge/charge curves at a current density of 0.1 A g^{-1}, (c) cycling performance at 1.0 A g^{-1}, and (d) rate performance.

could be observed near 0.35 and 0.55 V, corresponding to the transformation of Li_xSi into Si. In short, the peaks of the initial discharge-charge curves matched well with the CV curves. The initial discharge/charge capacities of Si-CNT/rGO/AC@PDC-30, Si-CNT/rGO/AC, and Si-CNT/AC microspheres obtained at 0.1 A g^{-1} were 3814/2791, 3184/2267, 2833/1949 mA h g^{-1} with initial Coulombic efficiencies (ICEs) of 73.2, 71.2, and 68.8 %, respectively. Si-CNT/rGO/AC microspheres exhibited higher ICEs and reversible capacities in comparison to the sample without rGO nanosheets due to the synergistic effect of 1D CNT and 2D graphene oxide materials. Compositing the two conductive carbon led to the formation of 3D conductive network that could accelerate the electron transport. Furthermore, by combining the two, comparatively denser structure was formed, which can enhance the contact with silicon. In addition, by forming a pitch-derived carbon coating at the interior and on the surface of the Si-CNT/rGO/AC microspheres, much denser structure is formed, resulting in the secured contact between Si and the conductive carbon materials. Such design of the anode material led to a high reversible capacity of 2791 mA h g^{-1} at 0.1 A g^{-1} and ICE of 73.2 %. The cycle performances of the three microspheres at a current density of 1.0 A g^{-1} are shown in Fig. 5c. The capacities of Si-CNT/rGO/AC@PDC-30, Si-CNT/rGO/AC, and Si-CNT/AC microspheres after 350 cycles at 1.0 A g^{-1} were 946.7, 677.9, and 457.4 mA h g^{-1}, respectively, where the capacity retention calculated from the 5th cycle was 60.1, 49.7, and 41.5 %, respectively. Si-CNT/rGO/AC microspheres exhibited higher cyclic stability in comparson to Si-CNT/AC microspheres, which is due to the rGO nanosheets that successfully encapsulated the Si nanoparticles as can be observed in Fig. 1d and alleviated the volume expansion during repetitive cycling. By reinforcing the structural robustness of Si-CNT/rGO/AC microspheres with pitch-derived carbon coating layer, much higher capacity retention as well as high capacity could be retained even after 350 cycles. To further investigate the structural merits of Si-CNT/rGO/AC@PDC-30 microspheres, rate capability of the prepared anode materials was tested and shown in Fig. 5d. At current densities of 0.1, 0.2, 0.5, 0.7, 1.0, 1.5, and 2.0 A g^{-1}, Si-CNT/rGO/AC@PDC-30 microspheres exhibited capacities of 3147, 2840, 2027, 1663, 1365, 890, and 617 mA h g^{-1}, respectively. Si-CNT/rGO/AC and Si-CNT/AC microspheres showed similar capacities until 0.7 A g^{-1}, but the capacity difference widened at higher current densities. The capacities obtained from the two anode materials were 451 and 290 mA h g^{-1}, respectively, at 2.0 A g^{-1}; electrode that combined rGO and CNT exhibited higher rate capability, which can be attributed to the well-formed 3D conductive matrix, which physically bound the two conductive carbons and facilitated electron transfer, accelerating the electrochemical kinetics. The highest capacity of 617 mA h g^{-1} could be obtained at 2.0 A g^{-1} for Si-CNT/rGO/AC@PDC-30 microspheres since the PDC coating made possible the densification of the anode so that the lithium-ion and electron transport could be both secured. This allowed the microspheres to play the role of a mixed ionic and electronic conductor (MIEC) which enables high rate capability. Additionally, the electrochemical performance of Si-CNT/rGO/AC@PDC-30 microspheres prepared in the present study is compared with other previously reported Si/carbon-based anodes in the Table S3. The superior Li-ion storage capability of Si-CNT/rGO/AC@PDC-30 microspheres compared to those of Si-CNT/rGO/AC and Si-CNT/AC microspheres could be elucidated by the EIS Nyquist plots shown in Fig. 6. The Nyquist plots of the microspheres were obtained after cell assembly (denoted as 'Fresh' in Fig. 6a), 7th cycle, and 200th cycles for the fully charged states. The obtained plots were further deconvoluted with the Randles-type equivalent circuits shown in Fig. S7. The Nyquist plots for the Fresh state showed only one semicircle since SEI layer was not formed on the surface of the anode, and therefore the circuit in Fig. S7a was used. On the other hand, Nyquist plots obtained after cycling revealed two semicircles that appear

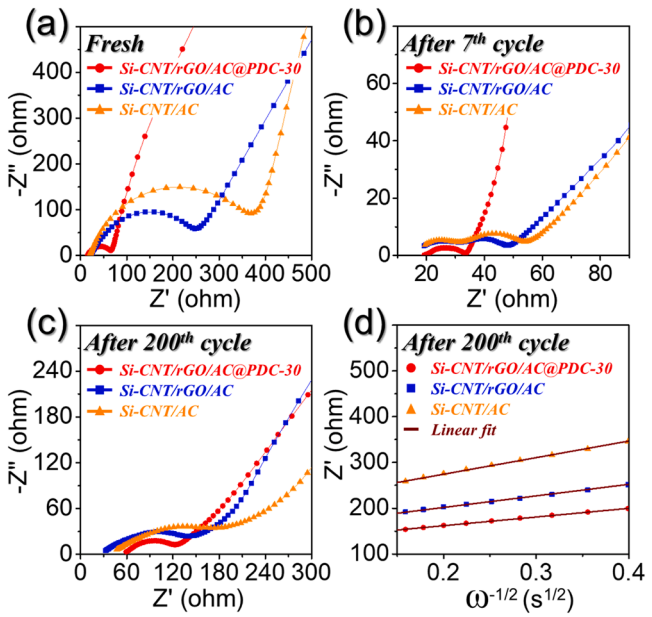

Fig. 6. Nyquist impedance plots of Si-CNT/rGO/AC@PDC-30, Si-CNT/rGO/AC, and Si-CNT/AC microspheres: (a) before cycling, (b) after 7th cycle, (c) after 200th cycle; (d) relationships between the real part of the impedance (Z_{re}) and $\omega^{-1/2}$ obtained after 200 cycles at 1.0 A g^{-1}.

at the high and middle frequency regions, which can be assigned to the resistance from the SEI layer (R_f) and charge transfer (R_{ct}), respectively, and therefore the circuit in Fig. S7b was utilized. R_{ct} values of the coin cells prior to cycling for Si-CNT/rGO/AC@PDC-30, Si-CNT/rGO/AC, and Si-CNT/AC microspheres were 57, 258, and 390 Ω, respectively (Table S4). Si-CNT/rGO/AC microspheres revealed lower R_{ct} values in comparison to Si-CNT/AC microspheres due to the synergistic effect of 3D conductive matrix that comprises 1D CNTs and 2D rGO nanosheets, which acted as conductive highways for the electron transport. R_{ct} values greatly reduced after coating conductive PDC layer on the surface since it densified the anode and made possible the compact electron transport pathways. After the 7th and 200th cycle, a consistant trend was observed, where the R_{ct} values of Si-CNT/rGO/AC@PDC-30 microspheres (12 and 80 Ω, respectively) remained the lowest among the three electrodes (Fig. 6b and c). Notably, the small-sized semicircle corresponding to R_f of Si-CNT/rGO/AC@PDC-30 anode after the 7th cycle shown in the magnified Nyquist plot (Fig. S8) indicates the formation of a thin and stable SEI layer on the surface. These results indicate that the structural advantages of Si-CNT/rGO/AC@PDC-30 microspheres not only facilitated the charge transfer kinetics and accelerated the electrochemical reactions, but also provided structural robustness which highly enhanced the electrode's durability during repetitive cycling. Additionally, Nyquist plots of all anodes after 200 cycles only exhibited one semicircle, which differs from the two semicircles observed after initial cycling, which can be attributed to the overlapping process and stabilization of the SEI layer. The stabilized SEI layer during long-term cycling leads to a reduction in its dynamic changes, subsequently, R_f can overlap with the R_{ct} in the middle frequency region, resulting in a single, dominant semicircle in the Nyquist plot [43,44]. Moreover, the stabilized SEI layer can reduce its distinguishable contribution to the impedance spectrum and effectively merges with the charge transfer impedance, simplifying the observed response [45]. For further investigation, the lithium-ion diffusivity of the three electrodes after the 200th cycle, as shown in Fig. 6d, was calculated according to the following equations, whose parameters are well-explained in the previous literatures [46]:

$$D_{Li^+} = 0.5R^2T^2 / A^2F^4C^2\sigma_w^2 \quad (1)$$

Here, R denotes the gas constant, T is the temperature, A represents the electrode area, C is the concentration of lithium ions, F stands for the Faraday constant, and σ_W corresponds to the Warburg impedance factor. The calculated D_{Li^+} values of Si-CNT/rGO/AC@PDC-30, Si-CNT/rGO/AC, and Si-CNT/AC microspheres after 200 cycles are provided in Table S4; Si-CNT/rGO/AC@PDC-30 showed twice the lithium-ion diffusivity of Si-CNT/rGO/AC, which in turn had twice the lithium-ion diffusivity of Si-CNT/AC microspheres. This again proved the merits of synergistic effect of compositing 1D CNTs and 2D rGO nanosheets and coating PDC layer, which can act as a MIEC for improving the performance of lithium-ion batteries.

To confirm the superior structural stability of Si-CNT/rGO/AC@PDC-30, the electrode surface of Si-CNT/rGO/AC@PDC-30, Si-CNT/rGO/AC, and Si-CNT/AC anodes were analyzed after 350th cycle at 1.0 A g^{-1} as shown in Fig. 7. Low-magnification FE-SEM images of the surface for Si-CNT/rGO/AC@PDC-30, Si-CNT/rGO/AC, and Si-CNT/AC anode after 350 cycles are showed in Fig. 7a, d, and g, respectively. The surface morphology of Si-CNT/rGO/AC@PDC-30 anode exhibits a relatively compact and stable structure (Fig. 7a). In contrast, electrode consisted of Si-CNT/rGO/AC microspheres, which lacks the protective PDC layer, reveals more prominent cracking across the surface (Fig. 7d), indicative of substantial structural degradation. Similarly, Si-CNT/AC microspheres, which excludes both rGO and the PDC protective layer, exhibits the most severe cracking and particle agglomeration among the samples, as shown in Fig. 7g. As can be shown in the higher-magnification FE-SEM images in Fig. 7b and c, independent microspherical morphologies could be retained after cycling, in case of Si-CNT/rGO/AC@PDC-30 microspheres. The FE-SEM images of Si-CNT/rGO/AC microspheres (Fig. 7e and f) indicate that the microspheres exhibit a certain degree of aggregation and coalescence during cycling, and this microstructural instability likely contributes to capacity fading. Si-CNT/AC microspheres showed a larger degree of particle agglomeration (Fig. 7h and i) since the absence of rGO led to weaker structural integrity, resulting in significant coalescence and loss of distinct microsphere morphology after cycling. Such structural breakdown suggests that Si-CNT/AC microspheres are more prone to mechanical failure and rapid capacity degradation during cycling. Overall, the comparison between the three anodes highlights the critical role of PDC coating and 3D rGO-CNT composite in enhancing the stability of the Si-based anode. Si-CNT/rGO/AC@PDC-30 anode demonstrates superior morphological stability, attributed to the synergistic effects of the conductive matrix and buffering layer of PDC, which together alleviate stress and prevent severe particle aggregation.

To analyze the practical usability of the Si-CNT/rGO/AC@PDC-30 anode, the electrochemical test of the full cell comprising the Si-CNT/rGO/AC@PDC-30 anode paired with $Li(Ni_{0.8}Co_{0.1}Mn_{0.1})O_2$ (NCM811) cathode were performed. Prior to the full-cell testing of the Si-CNT/rGO/AC@PDC-30 anode, Si-CNT/rGO/AC@PDC-30 microspheres were blended with commercial graphite, targeting practical applications in large-scale energy storage systems such as electric vehicles. These anodes were prepared with a 15:85 weight ratio of Si-CNT/rGO/AC@PDC-30 microspheres to commercial graphite, aligning with the blend ratio close to fourth-generation electric vehicles. The materials characteristics of the commercial graphite used for blending tests including FE-SEM and XRD analyses are presented in Fig. S9. Before electrochemical analysis of graphite-blended Si-CNT/rGO/AC@PDC-30 microspheres, the cycle performance of Si-CNT/rGO/AC@PDC-30 microspheres is tested under constant current-constant voltage (CC-CV) at a current density of 1.0 A g^{-1} mode as shown in Fig. S10a, where a high capacity retention could be observed after 50 cycles. As shown in Fig. S10b, the discharge capacity of graphite-blended Si-CNT/rGO/AC@PDC-30 microspheres for the 3rd cycle at 0.5 C (1.0 C = 680 mA g^{-1}) was 538 mA h g^{-1}, which is much higher than that of commercial graphite (361 mA h g^{-1}). The blended anode delivered a reversible discharge capacity of 500 mA h g^{-1} after 50 cycles at 0.5 C (1.0 C = 680 mA g^{-1}), which is 41 % higher than the 353 mA h g^{-1} achieved by

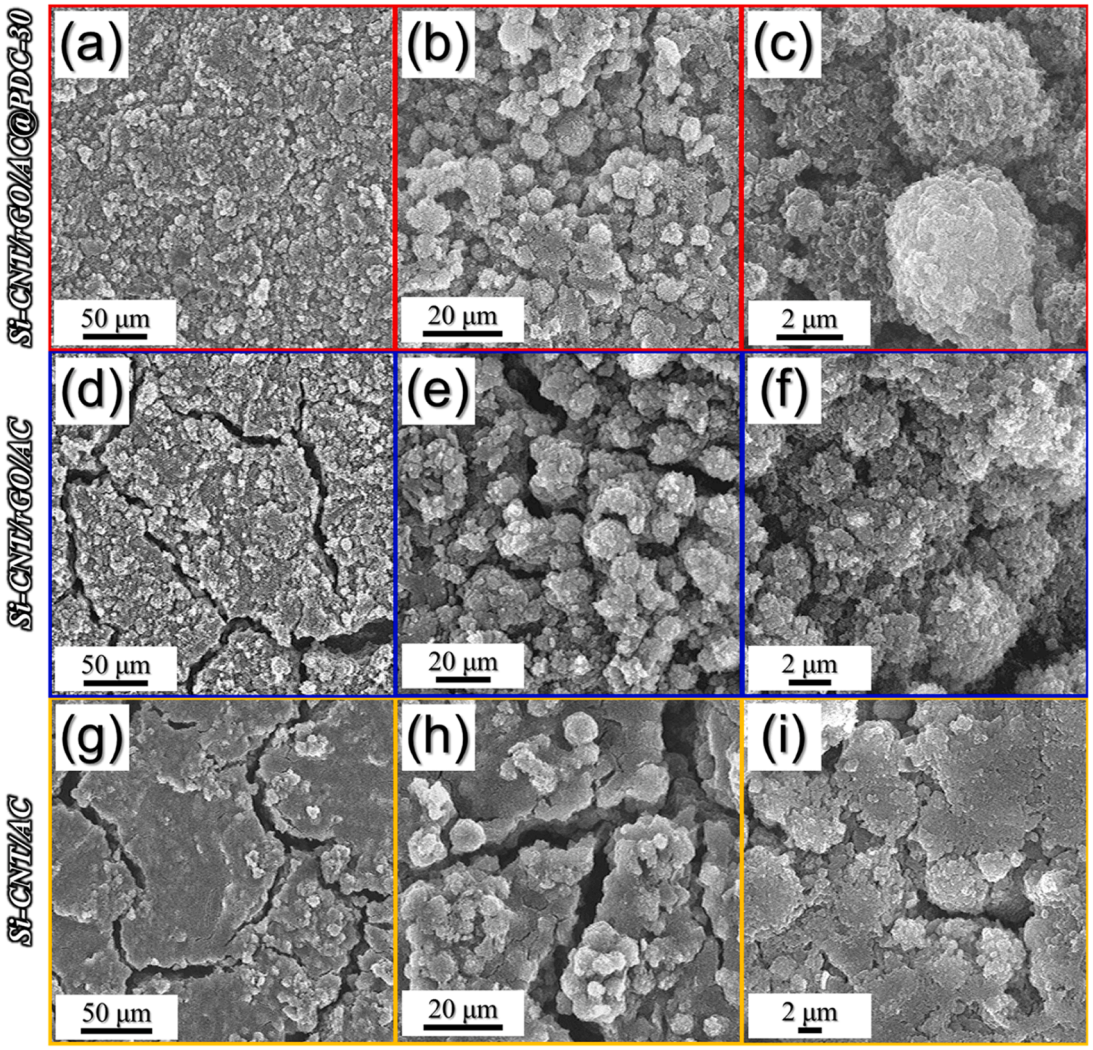

Fig. 7. Electrode surface of Si-CNT/rGO/AC@PDC-30, Si-CNT/rGO/AC, and Si-CNT/AC anodes obtained after 350th cycle at 1.0 A g^{-1}: (a–c) FE-SEM images of the Si-CNT/rGO/AC@PDC-30, (d–f) Si-CNT/rGO/AC, and (g–i) Si-CNT/AC.

commercial graphite. Additionally, the discharge capacities of the blended anodes consistently outperformed commercial graphite at various current densities (Fig. S10c). Moreover, the preliminary physical and electrochemical assessments of commercial NCM811 cathode were carried out before integration into a full cell setup, as shown in Fig. S11. The FE-SEM images revealed a non-aggregated spherical morphology of the NCM811 powder (Fig. S11a and b). The XRD pattern perfectly matched with the rhombohedral crystal structure with $R\bar{3}m$ space group (Fig. S11c). The half-cell cycle performance of the NCM811 cathode was shown in Fig. S11d, where it exhibited a discharge capacity of 156 mA h g^{-1} after 150 cycles at 0.5 C (1.0 C = 180 mA g^{-1}), when cycled in potential range of 2.7–4.3 V. Additionally, the NCM811 cathode demonstrated discharge capacities of 208, 196, 188, 177, 167, 153, 118, 89, and 60 mA h g^{-1} at 0.1, 0.2, 0.3, 0.5, 0.7, 1.0, 2.0, 3.0, and 5.0 C, respectively (Fig. S11e). Furthermore, full cells comprising commercial graphite-blended Si-CNT/rGO/AC@PDC-30 anode and commercial NCM811 cathode were assembled to evaluate the practical application potential of the prepared anode (Fig. S12). The full-cells were cycled within a voltage range of 1.5–4.2 V, with the active material loading masses of the anode and cathode set at approximately 4.3 and 12.3 mg cm^{-2}, respectively, ensuring an N/P ratio of ~1.1 to meet practical application conditions. The schematic configuration of NCM811//graphite-Si-CNT/rGO/AC@PDC-30 full cell is provided in Fig. S12a. Upon full charging up to 4.2 V at 0.1C, the full cell was able to power up a light-emitting diode (5 V, 10 mW), demonstrating its large-scale energy storage capability (Fig. S12b). The initial charge/discharge capacities of the full cell at 0.1 and 0.5 C were 216/195 mA h g^{-1} and 180/171 mA h g^{-1}, respectively, as shown in Fig. S12c. The cell retained a discharge capacity of 166 mA h g^{-1} after 50 cycles at 0.5 C, with a high coulombic efficiency (CE) of 99.9 %, indicating the robustness and practical feasibility of Si-CNT/rGO/AC@PDC-30 anodes (Fig. S12d). The full cell also exhibited high rate capability, where discharge capacities of 193, 184, 179, 162, 136, and 91 mA h g^{-1} could be delivered at 0.1, 0.2, 0.3, 0.5, 0.7, and 1.0 C, respectively (Fig. S12e). These results collectively highlight the practical application potential of Si-CNT/rGO/AC@PDC-30 anodes when paired with an NCM811 cathode.

4. Conclusions

In this study, an innovative design strategy for the synthesis of a three-dimensional conductive framework composed of 1D CNTs, 2D rGO, and amorphous carbon encapsulating Si nanoparticles, to which pitch-derived carbon layer is coated is reported. A one-pot spray drying of an aqueous colloidal solution containing CNTs, GO nanosheets, sucrose, and Si nanoparticles and one-step calcination process under N_2 atmosphere resulted in the formation of Si-CNT/rGO/AC microspheres. The resultant powder was mixed well with a THF solution that contains pitch carbon and subsequent carbonization process yielded Si-CNT/

rGO/AC@PDC microspheres. Different amount of pitch carbon was used to coat Si-CNT/rGO/AC microspheres to systematically understand the optimum amount of pitch carbon for achieving the best electrochemical performance, where 30 wt.% pitch was determined as the optimum value. When applied as the anode for LIBs, the microspheres exhibited a highly stable cycle performance where a discharge capacity of 947 mA h g^{-1} could be delivered after 350 cycles at 1.0 A g^{-1}. Combining the 1D structured CNTs and 2D rGO nanosheets formed denser structure in comparison to when using only CNTs and formed 3D conductive lithium and electron transport pathway for accelerating the charge transfer kinetics. The combined 3D framework also acted to effectively alleviate the volume changes that occur during cycling. PDC layer was formed at the interior and on the surface of the anode, which further reinforced the structural robustness and densified the electrode. It is believed that this design strategy for forming the 3D conductive composite with Si nanoparticles may pave the way towards significant advancements in lithium-ion batteries, enhancing their performance, durability, and energy density.

CRediT authorship contribution statement

Jae Seob Lee: Writing – original draft, Visualization, Software, Investigation, Data curation, Conceptualization. **Beom Su Jo:** Writing – original draft, Visualization, Investigation, Data curation, Conceptualization. **Jin-Sung Park:** Writing – review & editing, Writing – original draft, Supervision, Formal analysis, Conceptualization. **Jung Sang Cho:** Writing – review & editing, Supervision, Project administration, Funding acquisition, Conceptualization.

Declaration of competing interest

The authors declare that they have no known competing financial interests or personal relationships that could have appeared to influence the work reported in this paper.

Acknowledgments

This work was supported by the National Research Foundation of Korea (NRF) grant funded by the Korea government (MSIT) (Grant no.: RS-2023-00217581). Following are results of a study on the “Leaders in INdustry-university Cooperation 3.0” Project, supported by the Ministry of Education and National Research Foundation of Korea. This research was supported by Global - Learning & Academic Research Institution for Master’s·PhD Students, and Postdocs (G-LAMP) Program of the National Research Foundation of Korea (NRF) grant funded by the Ministry of Education (No. RS-2023-00285390).

Supplementary materials

Supplementary material associated with this article can be found, in the online version, at doi:10.1016/j.electacta.2024.145440.

Data availability

No data was used for the research described in the article.

References

[1] G. Harper, R. Sommerville, E. Kendrick, L. Driscoll, P. Slater, R. Stolkin, A. Walton, P. Christensen, O. Heidrich, S. Lambert, A. Abbott, K. Ryder, L. Gaines, P. Anderson, Recycling lithium-ion batteries from electric vehicles, Nature 575 (2019) 75–86, https://doi.org/10.1038/s41586-019-1682-5.

[2] P. Li, H. Kim, S.-T. Myung, Y.-K. Sun, Diverting exploration of silicon anode into practical way: a review focused on silicon-graphite composite for lithium ion batteries, Energy Storage Mater. 35 (2021) 550–576, https://doi.org/10.1016/j.ensm.2020.11.028.

[3] Q. Wang, M. Zhu, G. Chen, N. Dudko, Y. Li, H. Liu, L. Shi, G. Wu, D. Zhang, High-performance microsized Si anodes for lithium-ion batteries: insights into the polymer configuration conversion mechanism, Adv. Mater. 34 (2022) e2109658, https://doi.org/10.1002/adma.202109658.

[4] X. Li, M. Wu, T. Feng, Z. Xu, J. Qin, C. Chen, C. Tu, D. Wang, Graphene enhanced silicon/carbon composite as anode for high performance lithium-ion batteries, RSC Adv. 7 (2017) 48286–48293, https://doi.org/10.1039/C7RA09818A.

[5] P.U. Nzereogu, A.D. Omah, F.I. Ezema, E.I. Iwuoha, A.C. Nwanya, Anode materials for lithium-ion batteries: a review, Appl. Surf. Sci. Adv. 9 (2022) 100233, https://doi.org/10.1016/j.apsadv.2022.100233.

[6] X. Li, M. Zhang, S. Yuan, C. Lu, Research progress of silicon/carbon anode materials for lithium-ion batteries: structure design and synthesis method, ChemElectroChem 7 (2020) 4289–4302, https://doi.org/10.1002/celc.202001060.

[7] X. Zuo, J. Zhu, P. Müller-Buschbaum, Y.-J. Cheng, Silicon based lithium-ion battery anodes: a chronicle perspective review, Nano Energy 31 (2017) 113–143, https://doi.org/10.1016/j.nanoen.2016.11.013.

[8] G.G. Eshetu, E. Figgemeier, Confronting the challenges of next-generation silicon anode-based lithium-ion batteries: role of designer electrolyte additives and polymeric binders, ChemSusChem 12 (2019) 2515–2539, https://doi.org/10.1002/cssc.201900209.

[9] Y. Li, Q. Li, J. Chai, Y. Wang, J. Du, Z. Chen, Y. Rui, L. Jiang, B. Tang, Si-based anode lithium-ion batteries: a comprehensive review of recent progress, ACS Mater. Lett. 5 (2023) 2948–2970, https://doi.org/10.1021/acsmaterialslett.3c00253.

[10] L. Li, C. Fang, G. He, Y. Huang, Surface chemistry-controlled SEI layer on silicon electrodes by regulating electrolyte decomposition, ACS Appl. Mater. Interfaces 15 (2023) 36344–36355, https://doi.org/10.1021/acsami.3c07241.

[11] C. Zhang, F. Wang, J. Han, S. Bai, J. Tan, J. Liu, F. Li, Challenges and recent progress on silicon-based anode materials for next-generation lithium-ion batteries, Small. Struct. 2 (2021) 2100009, https://doi.org/10.1002/sstr.202100009.

[12] H.E. Kang, J. Ko, S.G. Song, Y.S. Yoon, Recent progress in utilizing carbon nanotubes and graphene to relieve volume expansion and increase electrical conductivity of Si-based composite anodes for lithium-ion batteries, Carbon 219 (2024) 118800, https://doi.org/10.1016/j.carbon.2024.118800.

[13] S. Suh, H. Choi, K. Eom, H.-J. Kim, Enhancing the electrochemical properties of a Si anode by introducing cobalt metal as a conductive buffer for lithium-ion batteries, J. Alloys Compd. 827 (2020) 154102, https://doi.org/10.1016/j.jallcom.2020.154102.

[14] Y. Yu, C. Yang, Y. Jiang, J. Zhu, Y. Zhao, S. Liang, K. Wang, Y. Zhou, Y. Liu, J. Zhang, M. Jiang, Sponge-like porous-conductive polymer coating for ultrastable silicon anodes in lithium-ion batteries, Small 19 (2023) e2303779, https://doi.org/10.1002/smll.202303779.

[15] J. Zhou, N. Lin, Y. Han, J. Zhou, Y. Zhu, J. Du, Y. Qian, Cu_3Si@Si core-shell nanoparticles synthesized using a solid-state reaction and their performance as anode materials for lithium ion batteries, Nanoscale 7 (2015) 15075–15079, https://doi.org/10.1039/C5NR04456A.

[16] P. Bhattacharya, D.H. Suh, P. Nakhanivej, Y. Kang, H.S. Park, Iron oxide nanoparticle-encapsulated CNT branches grown on 3D ozonated CNT internetworks for lithium-ion battery anodes, Adv. Funct. Mater. 28 (2018) 1801746, https://doi.org/10.1002/adfm.201801746.

[17] J.S. Yeon, Y.H. Ko, T.H. Park, H. Park, J. Kim, H.S. Park, Multidimensional hybrid architecture encapsulating cobalt oxide nanoparticles into carbon nanotube branched nitrogen-doped reduced graphene oxide networks for lithium-sulfur batteries, Energy Environ. Mater. 5 (2021) 555–564, https://doi.org/10.1002/eem2.12187.

[18] P. Nie, Z. Le, G. Chen, D. Liu, X. Liu, H.B. Wu, P. Xu, X. Li, F. Liu, L. Chang, X. Zhang, Y. Lu, Graphene caging silicon particles for high-performance lithium-ion batteries, Small 14 (2018) e1800635, https://doi.org/10.1002/smll.201800635.

[19] H. Tang, Y.J. Zhang, Q.Q. Xiong, J.D. Cheng, Q. Zhang, X.L. Wang, C.D. Gu, J. P. Tu, Self-assembly silicon/porous reduced graphene oxide composite film as a binder-free and flexible anode for lithium-ion batteries, Electrochim. Acta 156 (2015) 86–93, https://doi.org/10.1016/j.electacta.2015.01.009.

[20] Q. Zhang, B. Xi, W. Chen, J. Feng, Y. Qian, S. Xiong, Synthesis of carbon nanotubes-supported porous silicon microparticles in low-temperature molten salt for high-performance Li-ion battery anodes, Nano Res. 15 (2022) 6184–6191, https://doi.org/10.1007/s12274-022-4275-9.

[21] Q. Wei, G.-C. Liu, C. Zhang, X.-J. Hong, C.-L. Song, Y. Yang, M. Zhang, W. Huang, Y.-P. Cai, Novel honeycomb silicon wrapped in reduced graphene oxide/CNT system as high-stability anodes for lithium-ion batteries, Electrochim. Acta 317 (2019) 583–593, https://doi.org/10.1016/j.electacta.2019.06.024.

[22] S.H. Choi, G. Nam, S. Chae, D. Kim, N. Kim, W.S. Kim, J. Ma, J. Sung, S.M. Han, M. Ko, H.W. Lee, J. Cho, Robust pitch on silicon nanolayer-embedded graphite for suppressing undesirable volume expansion, Adv. Energy Mater. 9 (2018) 1803121, https://doi.org/10.1002/aenm.201803121.

[23] F. Wu, Y. Dong, Y. Su, C. Wei, T. Chen, W. Yan, S. Ma, L. Ma, B. Wang, L. Chen, Q. Huang, D. Cao, Y. Lu, M. Wang, L. Wang, G. Tan, J. Wang, N. Li, Benchmarking the effect of particle size on silicon anode materials for lithium-ion batteries, Small 19 (2023) e2301301, https://doi.org/10.1002/smll.202301301.

[24] S.N. Alam, N. Sharma, L. Kumar, Synthesis of graphene oxide (GO) by modified hummers method and its thermal reduction to obtain reduced graphene oxide (rGO), Graphene 6 (2017) 1–18, https://doi.org/10.4236/graphene.2017.61001.

[25] H. Chen, Z. Wang, X. Hou, L. Fu, S. Wang, X. Hu, H. Qin, Y. Wu, Q. Ru, X. Liu, S. Hu, Mass-producible method for preparation of a carbon-coated graphite@plasma nano-silicon@carbon composite with enhanced performance as lithium ion battery anode, Electrochim. Acta 249 (2017) 113–121, https://doi.org/10.1016/j.electacta.2017.07.146.

[26] S. Chae, Y. Xu, R. Yi, H.S. Lim, D. Velickovic, X. Li, Q. Li, C. Wang, J.G. Zhang, A micrometer-sized silicon/carbon composite anode synthesized by impregnation of petroleum pitch in nanoporous silicon, Adv. Mater. 33 (2021) e2103095, https://doi.org/10.1002/adma.202103095.
[27] J.S. Lee, R. Saroha, J.S. Cho, Porous microspheres comprising $CoSe_2$ nanorods coated with N-doped graphitic C and polydopamine-derived C as anodes for long-lived Na-ion batteries, Nano-Micro Lett. 14 (2022) 113, https://doi.org/10.1007/s40820-022-00855-z.
[28] L. Ma, X. Fu, F. Zhao, L. Yu, W. Su, L. Wei, G. Tang, Y. Wang, F. Wu, X. Guo, Microsized silicon/carbon composite anodes through in situ polymerization of phenolic resin onto silicon microparticles for high-performance lithium-ion batteries, ACS Appl. Energy Mater. 6 (2023) 4989–4999, https://doi.org/10.1021/acsaem.3c00534.
[29] H. Shi, W. Zhang, D. Wang, J. Wang, C. Wang, Z. Xiong, F.-R. Chen, H. Dong, B. Xu, X. Yan, Facile preparation of silicon/carbon composite with porous architecture for advanced lithium-ion battery anode, J. Electroanal. Chem. 937 (2023) 117427, https://doi.org/10.1016/j.jelechem.2023.117427.
[30] W. Xiao, Y. Qiu, Q. Xu, J. Wang, C. Xie, J. Peng, J. Hu, J. Zhang, X. Li, Building sandwich-like carbon coated Si@CNTs composites as high-performance anode materials for lithium-ion batteries, Electrochim. Acta 364 (2020) 137278, https://doi.org/10.1016/j.electacta.2020.137278.
[31] Y. Liu, X. Liu, Y. Zhu, J. Wang, W. Ji, X. Liu, Scalable synthesis of pitch-coated nanoporous Si/graphite composite anodes for lithium-ion batteries, Energy Fuels 37 (2023) 4624–4631, https://doi.org/10.1021/acs.energyfuels.2c03702.
[32] L. Niu, Q. Zhang, R. Zhang, D. Wang, G. Wen, L.-C. Qin, Modulating functional groups of GO to improve the electrochemical performance of Si/rGO anode, Colloids Surf. A 691 (2024) 133877, https://doi.org/10.1016/j.colsurfa.2024.133877.
[33] G. Zheng, Y. Xiang, L. Xu, H. Luo, B. Wang, Y. Liu, X. Han, W. Zhao, S. Chen, H. Chen, Q. Zhang, T. Zhu, Y. Yang, Controlling surface oxides in Si/C nanocomposite anodes for high-performance Li-ion batteries, Adv. Energy Mater. 8 (2018) 1801718, https://doi.org/10.1002/aenm.201801718.
[34] S.H. Oh, S.M. Park, D.-W. Kang, Y.C. Kang, J.S. Cho, Fibrous network of highly integrated carbon nanotubes/MoO_3 composite bundles anchored with MoO_3 nanoplates for superior lithium ion battery anodes, J. Ind. Eng. Chem. 83 (2020) 438–448, https://doi.org/10.1016/j.jiec.2019.12.017.
[35] R. Saroha, H.H. Choi, J.S. Cho, Boosting redox kinetics using rationally engineered cathodic interlayers comprising porous rGO-CNT framework microspheres with $NiSe_2$-core@N-doped graphitic carbon shell nanocrystals for stable Li-S batteries, Chem. Eng. J. 473 (2023) 145391, https://doi.org/10.1016/j.cej.2023.145391.
[36] R. Saroha, H.S. Ka, G.D. Park, C. Cho, D.-W. Kang, J.S. Cho, Long-term stability of lithium-sulfur batteries via synergistic integration of nitrogen-doped graphitic carbon-coated cobalt selenide nanocrystals within porous three-dimensional graphene-carbon nanotube microspheres, J. Power Sources 592 (2024) 233893, https://doi.org/10.1016/j.jpowsour.2023.233893.
[37] S. Yin, D. Zhao, Q. Ji, Y. Xia, S. Xia, X. Wang, M. Wang, J. Ban, Y. Zhang, E. Metwalli, X. Wang, Y. Xiao, X. Zuo, S. Xie, K. Fang, S. Liang, L. Zheng, B. Qiu, Z. Yang, Y. Lin, L. Chen, C. Wang, Z. Liu, J. Zhu, P. Muller-Buschbaum, Y.J. Cheng, Si/Ag/C nanohybrids with in situ incorporation of super-small silver nanoparticles: tiny amount, huge impact, ACS Nano 12 (2018) 861–875, https://doi.org/10.1021/acsnano.7b08560.
[38] R. Gao, J. Tang, K. Zhang, K. Ozawa, L.-C. Qin, A sandwich-like silicon–carbon composite prepared by surface-polymerization for rapid lithium-ion storage, Nano Energy 78 (2020) 105341, https://doi.org/10.1016/j.nanoen.2020.105341.
[39] H.-J. Shin, J.-Y. Hwang, H.J. Kwon, W.-J. Kwak, S.-O. Kim, H.-S. Kim, H.-G. Jung, Sustainable encapsulation strategy of silicon nanoparticles in microcarbon sphere for high-performance lithium-ion battery anode, ACS Sustain. Chem. Eng. 8 (2020) 14150–14158, https://doi.org/10.1021/acssuschemeng.0c04828.
[40] A. Nulu, V. Nulu, K.Y. Sohn, Silicon and porous MWCNT composite as high capacity anode for lithium-ion batteries, Korean J. Chem. Eng. 37 (2020) 1795–1802, https://doi.org/10.1007/s11814-020-0559-5.
[41] X. Shen, D. Mu, S. Chen, B. Xu, B. Wu, F. Wu, Si/mesoporous carbon composite as an anode material for lithium ion batteries, J. Alloys Compd. 552 (2013) 60–64, https://doi.org/10.1016/j.jallcom.2012.10.094.
[42] A. Thapa, H. Gao, Silicon-based anode and its full-cell performance test using a high-capacity pouch cell, J. Electrochem. Soc. 171 (2024) 010504, https://doi.org/10.1149/1945-7111/ad1630.
[43] N. Kakati, K. Lee, Y.S. Yoon, Synthesis of $ZnNiSnO_4$ nanorods by a simple hydrothermal method as a new anode material for Li ion battery, J. Alloys Compd. 711 (2017) 387–394, https://doi.org/10.1016/j.jallcom.2017.04.01.
[44] S.Y. Yang, J.S. Park, J.H. Kim, M. Yoon, S.E. Wang, D.S. Jung, Y.C. Kang, Spray-assisted synthesis of ant-cave-structured Ni-rich cathode microspheres with Li-reactive coating layer for high-performance Li-ion batteries, Mater. Today Chem. 35 (2024) 101889, https://doi.org/10.1016/j.mtchem.2023.101889.
[45] M.V. Reddy, T. Yu, C.H. Sow, Z.X. Shen, C.T. Lim, G.V. Subba Rao, B.V. R. Chowdari, α-Fe_2O_3 nanoflakes as an anode material for Li-ion batteries, Adv. Funct. Mater. 17 (2007) 2792–2799, https://doi.org/10.1002/adfm.200601186.
[46] J.S. Lee, R. Saroha, J.H. Oh, C. Cho, B. Jin, D.-W. Kang, J.S. Cho, Camphene-derived hollow and porous nanofibers decorated with hollow NiO nanospheres and graphitic carbon as anodes for efficient lithium-ion storage, J. Ind. Eng. Chem. 114 (2022) 276–287, https://doi.org/10.1016/j.jiec.2022.07.017.